MCAT Institute Final Report 90-001

Development of a Time-Dependent Incompressible Navier-Stokes Solver Based on a Fractional-Step Method

Moshe Rosenfeld

September 1990

MCAT Institute
San Jose, California

MCAT Institute Final Report 90-001

Development of a Time-Dependent Incompressible Navier-Stokes Solver Based on a Fractional-Step Method

Moshe Rosenfeld

FINAL REPORT
FOR THE PERIOD OCTOBER 1, 1988 TO FEBRUARY 15, 1990

September 1990

MCAT Institute
3933 Blue Gum Drive
San Jose, California 95127

DEVELOPMENT OF A TIME-DEPENDENT INCOMPRESSIBLE NAVIER-STOKES SOLVER BASED ON A FRACTIONAL-STEP METHOD

Moshe Rosenfeld

INTRODUCTION

This study has been focused on the development, validation and application of a fractional step solution method of the time-dependent incompressible Navier-Stokes equations in generalized coordinate systems. A solution method that combines a finite-volume discretization with a novel choice of the dependent variables and a fractional step splitting to obtain accurate solutions in arbitrary geometries has been previously developed for fixed-grids, see Ref. (1).

In the present research effort, this solution method is extended to include more general situations, including cases with moving grids. The numerical techniques are enhanced to gain efficiency and generality. This report summarizes briefly the work performed during the period October 1, 1988 through February 15, 1990. Additional details on the various aspects of the study are given in Appendix A.

NUMERICAL ENHANCEMENTS

The fixed grid solution method has been extended to general moving grids. Errors originating from the discrete approximation of the time-dependent coordinate system are minimized by satisfying the discrete geometric conservation laws for the time-varying computational cells. To improve the efficiency of the fixed grid case, two versions of the solution method have been coded: (1) fixed-grid method, (2) moving-grid method.

During the present study, several enhancements of the numerical method have been introduced. A partial list of the modifications is given below:

(1) Implementation of more general boundary conditions implicitly. The allowable boundary conditions are:

(a) Periodic conditions,
(b) Symmetric conditions,
(c) Mixed Dirichlet and Neumann type boundary conditions.

(2) The solution method has been extended to geometrically singular boundaries for the three types of grid topologies (C, O or H grids).

(3) A multi-grid Poisson solver has been written and partially debugged.

(4) Extensive efforts have been made to increase the efficiency of the method by improved vectorization. Presently, the fixed-grid method runs at 80 MFLOPS on the CRAY YMP (single CPU) and about 300 - 400 . 10^{-6} CPU sec/mesh-point/time-step are consumed. The moving-grid code is not yet fully vectorized.

VALIDATION OF THE METHOD

Several additional cases have been solved to validate the method against other numerical and experimental results. In all the cases tested so far, good agreement is obtained. The validation cases include:

Fixed-Grid Case:

(1) Flow in a two-dimensional polar cavity.

(2) Flow in a two-dimensional channel with a fixed constriction and a time variable pressure gradient.

(3) Flow over a two-dimensional elliptic airfoil with a steady and pulsatile upstream flow and a high laminar Reynolds number (Re = 14,300).

(4) Three-dimensional flow in curved ducts, both with rectangular and circular cross-sections.

(5) Flow over a submarine body at an incidence of 0^{o} and 20^{o}.

Additional details of these validation cases can be found in Ref. (2). A brief summary of preliminary results for two validation cases is given below:

Flow Over an Elliptical Airfoil at a High Reynolds Number

The two-dimensional flow over an elliptical airfoil of thickness ratio 1:2.91 at 14^{o} angle of attack and a Reynolds number of 14,300 has been solved to compare with the recent experimental results. Two cases have been considered, (a) steady upstream flow, (b) pulsatile upstream flow. In the second case, a sinusoidally pusatile upstream flow with an amplitude of 5% of the steady part, and a non-dimensional period of T = 6.86 was simulated. A non-orthogonal 0-type grid of 161 x 141 mesh points in the radial and circumferential directions, respectively, has been used. Figure 1 gives the time-evolution of the lift and drag coefficients for the steady and pulsatile upstream flows (it should be noted that in the pulsating case, the time is normalized by the period time T). The analysis of the results and the comparisons with the experimental results will be reported elsewhere.

Flow Over a Submarine Body at Low Reynolds Numbers

The axisymmetric flow over a submarine body has been computed for a low Reynolds number of Re = 1000 and a zero angle of attack. Figure 2 compares the pressure coefficient on the body of the submarine with the computed results of Ryan (Private Communication), while Fig. 3 shows the effect of the Reynolds number on the pressure coefficient. Figure 4 shows the distribution of the pressure coefficient for an incidence of 20^{o}. Figure 5 plots, for the same case, the limiting streamlines (viewed from the rear end of the submarine) and the particle traces (side view).

Moving-Grid Case:

(1) Flow over a circular cylinder with a moving outer boundary.

(2) Flow in a two-dimensional channel with a moving constriction.

(3) Flow in a two-dimensional cavity with a moving piston.

Additional details on these validation cases can be found in Appendix A.

CONCLUDING REMARKS

In the present study, a fractional step solution method of the time-dependent, viscous and incompressible Navier-Stokes equations has been extended, enhanced and validated for both fixed and moving generalized coordinate systems. The method has been used to simulate time-periodic vortical flow fields. Investigation of these flows by novel analysis methods that are being developed by the author, may advance the understanding of the complex vortical flow phenomena found in pulsating flows.

The study has demonstrated the capabilities of the present fractional solution method in simulating accurately complicated incompressible time-dependent viscous flow fields.

REFERENCES

1. Rosenfeld, M., Kwak, D., and Vinokur, M., "A Solution Method for the Unsteady and Incompressible Navier-Stokes Equations in Generalized Coordinate Systems," AIAA 26th Aerospace Sciences Meeting, January 1988, Reno, Nevada, AIAA paper 88-0718.

2. Rosenfeld, M., Kwak, D., and Vinokur, M., "A Fractional-Step Solution Method for the Unsteady Incompressible Navier-Stokes Equations in Generalized Coordinate Systems," *J. Comp. Physics,* submitted after revision, 1989.

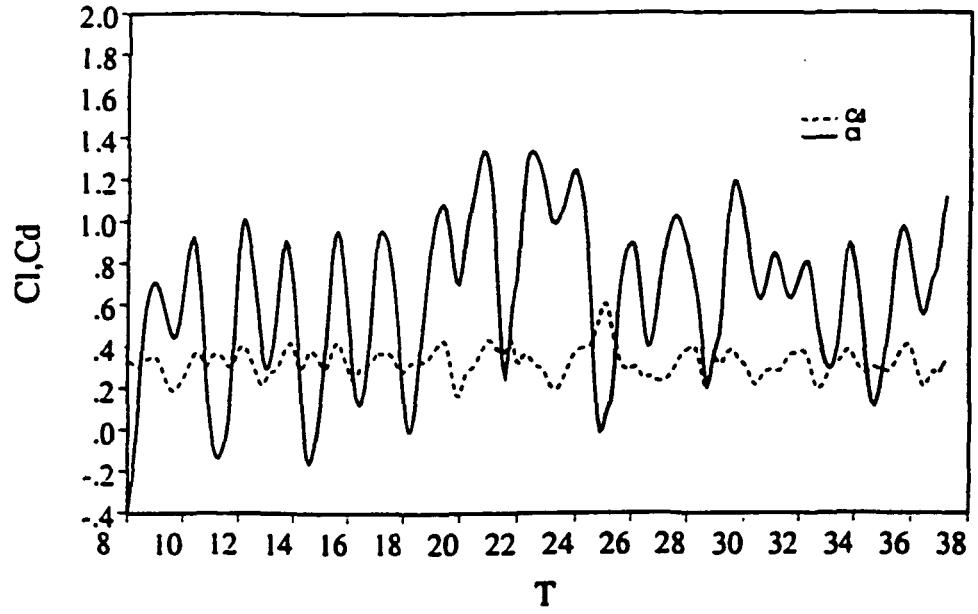

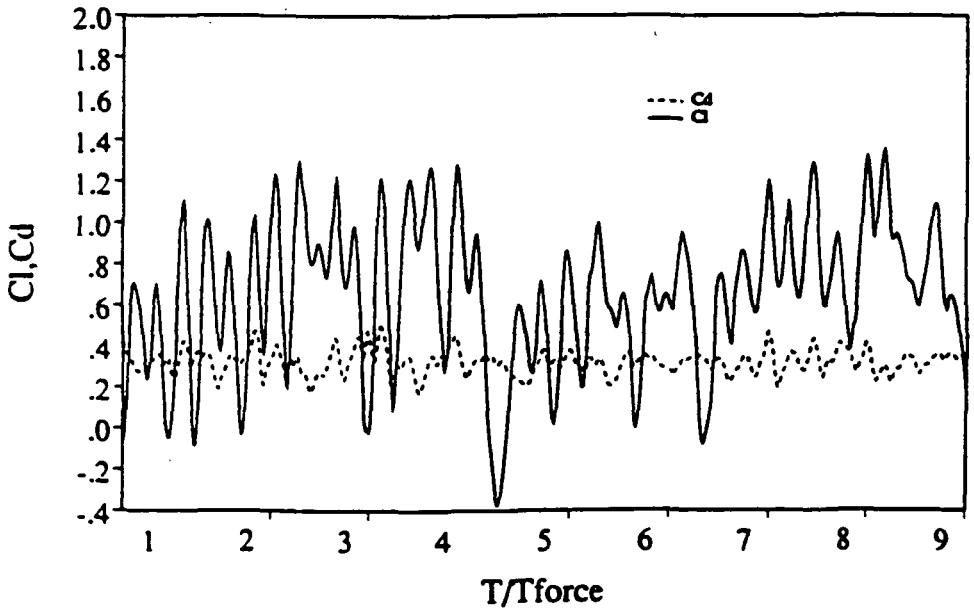

Fig. 1 - Time evolution of the force-coefficients on an elliptic cylinder at 14^{o} incidence and Re = 14,300.

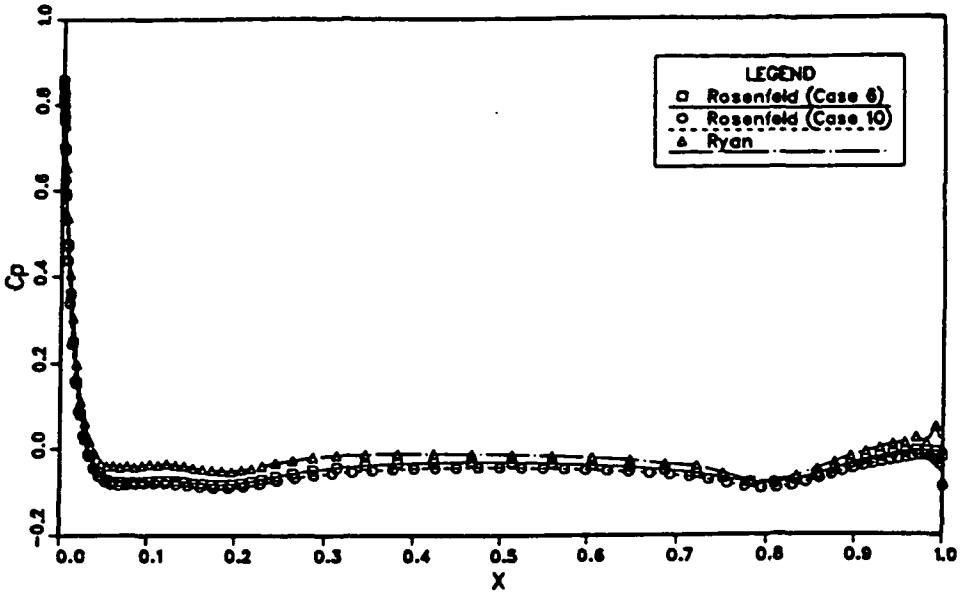

Fig. 2 - Distribution of the pressure-coefficient on the submarine body at 0° incidence.

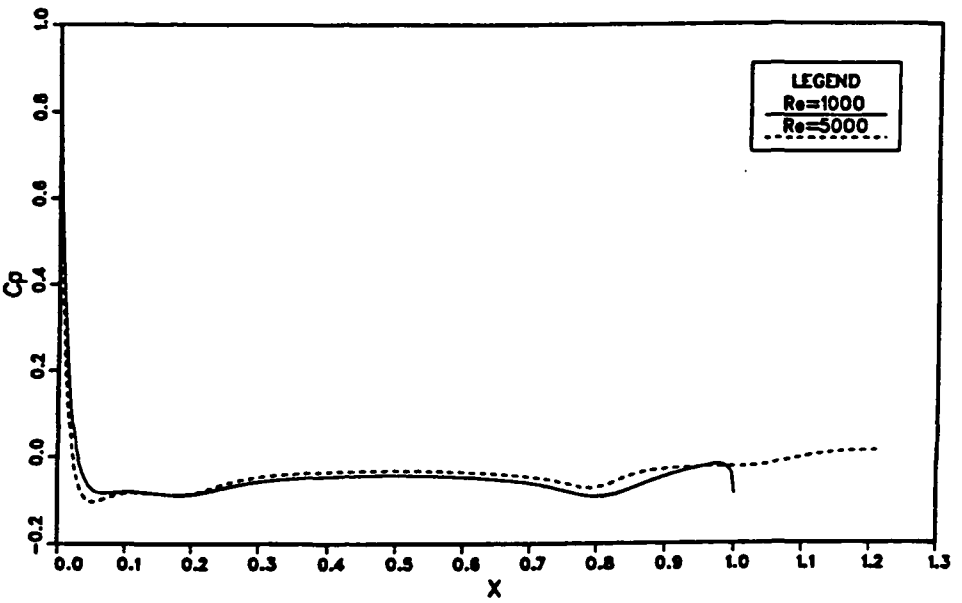

Fig. 3 - Effect of Reynolds number on the pressure-coefficient on submarine body at 0° incidence.

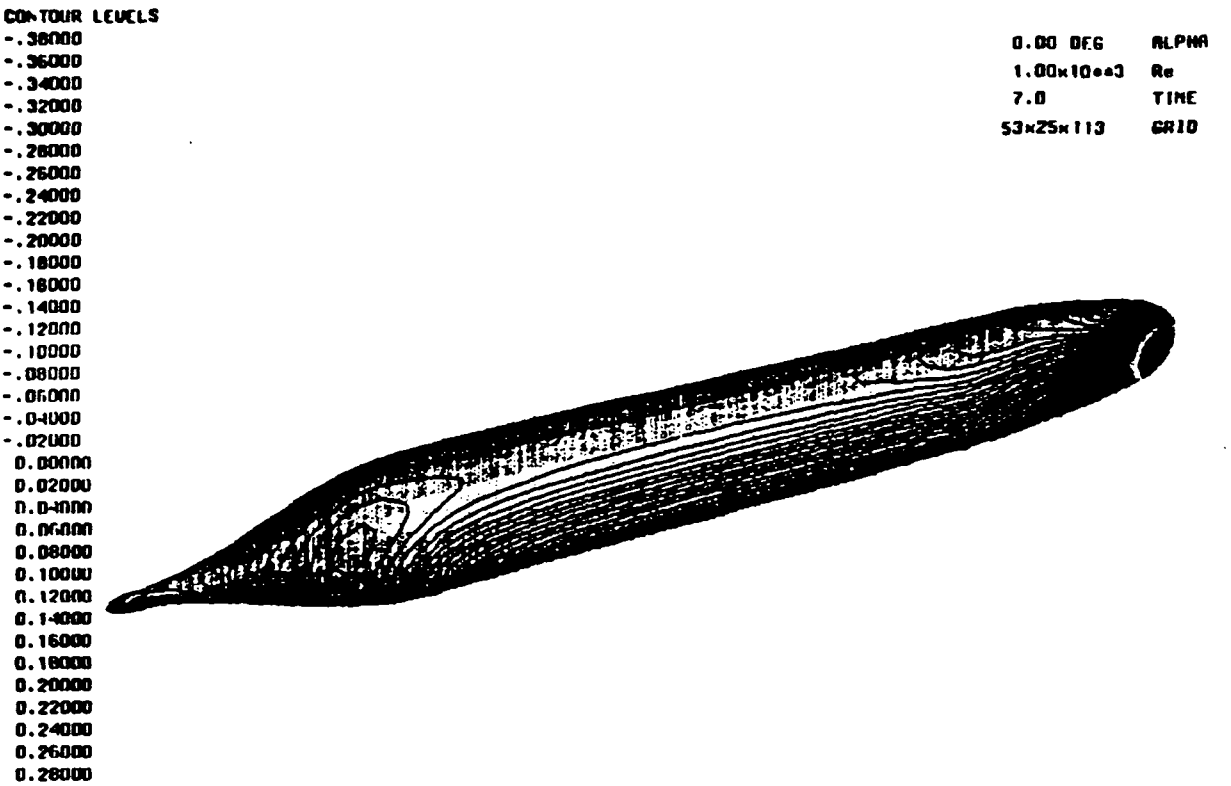

Fig. 4 - Distribution of the pressure-coefficient on the submarine body at 20^{o} incidence.

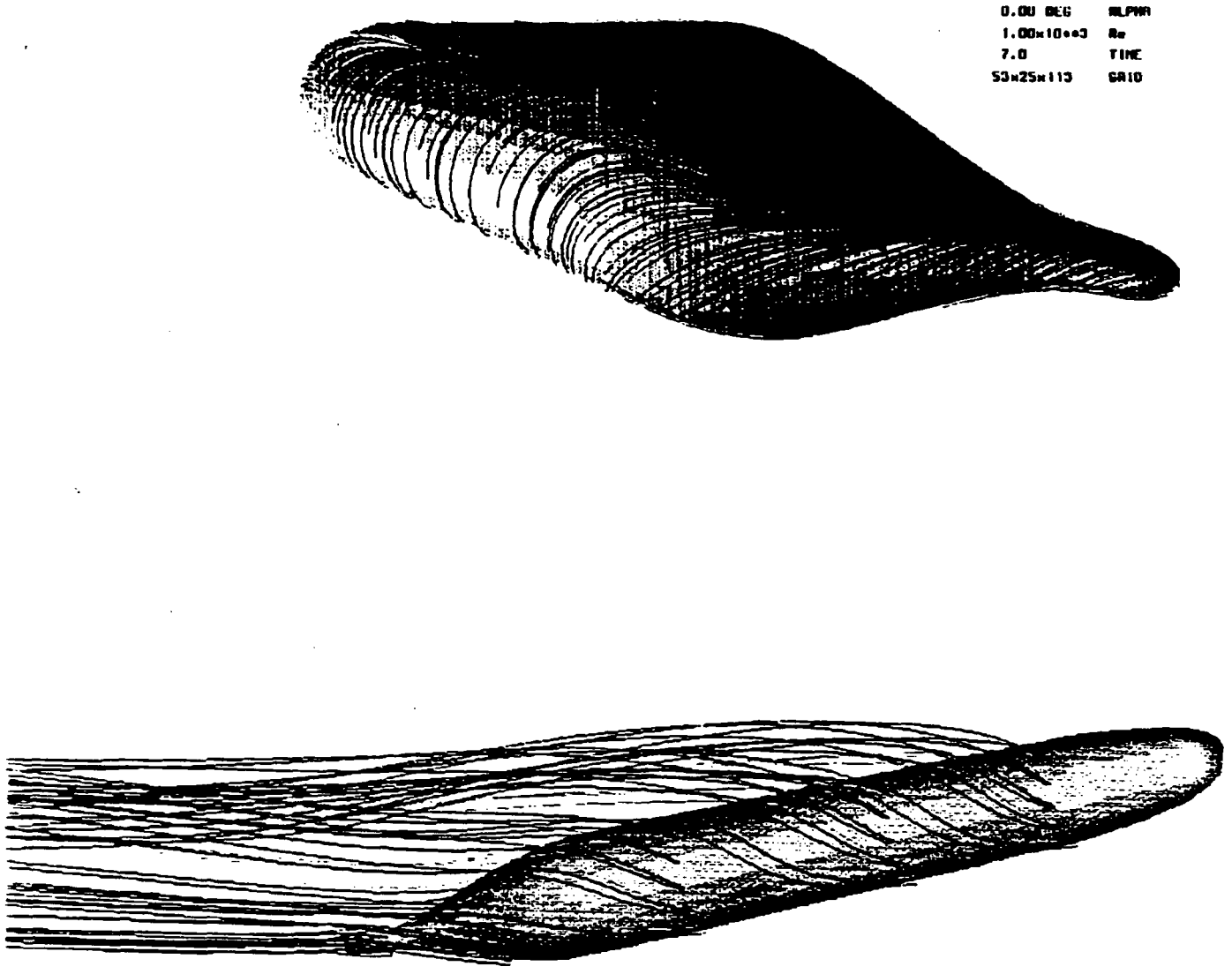

Fig. 5 - Limiting streamlines and particle traces for the submarine body at 20° incidence.

APPENDIX A

AIAA '89

AIAA 89-0466
Numerical Solution of Unsteady Incompressible Viscous Flows in Generalized Moving Coordinate Systems

M. Rosenfeld and D. Kwak, NASA-Ames,
Moffett Field, CA

27th Aerospace Sciences Meeting
January 9–12, 1989/Reno, Nevada

NUMERICAL SOLUTION OF UNSTEADY INCOMPRESSIBLE VISCOUS FLOWS IN GENERALIZED MOVING COORDINATE SYSTEMS

Moshe Rosenfeld* and Dochan Kwak†
NASA Ames Research Center, Moffett Field, CA 94035

Abstract

A solution method of the time-accurate, incompressible Navier-Stokes equations in generalised curvilinear moving coordinate systems is presented in this paper. Accuracy is achieved by a conservative finite-volume discretisation which satisfies the geometric conservation laws in generalised moving coordinate systems. The solution method is second-order accurate in space and first-order accurate in time. A fractional step solution method is used to efficiently solve the discrete equations. The unknowns, namely the *pressure* and the *volume-fluxes*, are chosen to facilitate the formulation of a consistent Poisson equation and to obtain a robust Poisson solver with favorable convergence properties. The method is validated by comparisons to other numerical and experimental solutions. The comparisons show good agreement.

1 Introduction

Numerous solutions have already been obtained for steady, incompressible flows in complicated three-dimensional configurations, see for example Kwak *et al.*[1]. Time-dependent, viscous simulations require large computational resources and only recently, with the advent of new and large supercomputers, has their solution become feasible for complicated flow problems. However, the majority of the existing studies consider cases where a fixed grid can be employed. In many realistic situations one or more boundaries move and therefore the choice of a fixed grid is inadequate. Moving boundaries can be found in internal flows with a moving piston, bio-fluid flows with elastic boundaries as in cardiac flows, as well as in external aerodynamics where the contour of the configuration may deform either due to forced motion of the controls or aero-elastic interactions. Another circumstance which requires the use of moving grids is the application of adaptive grids to the solution of time-dependent flowfields.

Very few flow solutions exist for cases with moving grids. Ogawa and Ishiguro[2] solved a two-dimensional model of the blood flow in a human ventricle and the dynamic stall process on an oscillating airfoil by employing moving grids in a stream-function-vorticity formulation. Tamura *et al.*[3] have solved the two-dimensional flow over a circular cylinder with forced vibrations and with vortex-induced vibrations using primitive variables. Rogers and Kwak[4] have recently extended their time-accurate high-order upwind solution procedure, based on the artificial compressibility method (see Ref. [5]), to moving grids. This method was applied to the solution of the three-dimensional flowfield in a model of the artificial-heart developed by Pennsylvania State University. Kiris and Rogers[6] used this method to solve the internal flow in a cavity with a periodically moving piston. A somewhat restricted application of moving grids was used by Ralph and Pedley[7] to solve the flow in a two-dimensional channel with a moving indentation. The numerical method uses the stream-function-vorticity formulation and employs a specially devised time-dependent coordinate transformation to resolve the difficulties associated with the moving boundary. However, this procedure can be used only for a particular class of problems and can not be applied for more general cases where the mesh points may move arbitrarily.

In all these works a finite-difference approach is used. The grid's motion is accounted for by terms derived from the time-derivatives of the coordinate system. The finite volume approach to the discretization of the incompressible Navier-Stokes equations offers flexibility in applying certain geometric conservation laws and minimising the truncation errors in complicated geometries. In the finite volume discretisation methodology the geometric parameters have clear meaning such as the volume and faces' area of the computational cells.

In the present work, a fractional step solution procedure is developed for the time-dependent, incompressible, viscous flows in generalised moving coordinate systems. The formulation of the governing equations, the discretisation process and the numerical solution phases are combined together to yield an accurate solution method

*Senior Scientist, MCAT Institute, Member AIAA
†Research Scientist, Member AIAA

for complicated flow problems. Special attention is given to the satisfaction of the "geometric conservation laws" (both in space and time) to minimise the discretisation errors in complicated coordinate systems. This work emphasises the development of a conservative finite-volume formulation for moving grids with an efficient fractional step solution method based on a robust Poisson solver. Details pertaining to the fixed grid solution method can be found in other publications by the present authors.[8,9]

2 Formulation

The equations governing the flow of isothermal, constant density incompressible, viscous fluids in a time-dependent control volume with the face $S(t)$ and volume $V(t)$ are the conservation of mass

$$\frac{\partial V}{\partial t} + \oint_S d\mathbf{S} \cdot (\mathbf{u} - \mathbf{v}) = 0 \,, \tag{1}$$

and the conservation of momentum

$$\frac{\partial}{\partial t} \int_V \mathbf{u}\, dV = \oint_S d\mathbf{S} \cdot \bar{T} \,, \tag{2}$$

where t is the time, $\mathbf{u}$ is the velocity vector, $d\mathbf{S}$ is a surface area element and dV is a volume element. The surface element velocity resulting from the motion of the grid is $\mathbf{v}$. The tensor $\bar{T}$ is given by

$$\bar{T} = -(\mathbf{u} - \mathbf{v})\mathbf{u} - P\bar{I} + \nu\left(\nabla\mathbf{u} + (\nabla\mathbf{u})^T\right) \tag{3}$$

for Newtonian fluids. The quantity $\bar{I}$ is the identity tensor, $\nabla\mathbf{u}$ is the gradient of $\mathbf{u}$ while $(\cdot)^T$ is the transpose operator. The pressure is P, and ν is the effective kinematic viscosity.

The only differences between the fixed and the moving grid equations are the terms that include the surface element velocity $\mathbf{v}$ and the time dependence of the cell geometry (volume and face). The volume conservation of each time-varying cell (special case of (1)) requires

$$\frac{\partial V}{\partial t} - \oint_S d\mathbf{S} \cdot \mathbf{v} = 0 \,. \tag{4}$$

where the term $d\mathbf{S} \cdot \mathbf{v}$ represents the volume swept out by the face $d\mathbf{S}$ over the time increment dt. Thus, the mass conservation equation has exactly the same form as for fixed grids

$$\oint_S d\mathbf{S} \cdot \mathbf{u} = 0 \,, \tag{5}$$

The usual practise is to transform equations (2) and (5) into a differential form. In the present work the integral formulation is maintained to assist in the derivation of the finite-volume equations for obtaining a conservative scheme for arbitrarily moving geometries.

3 Discretization

3.1 Geometric Quantities

A general nonorthogonal coordinate system (ξ, η, ζ) is defined (discretely) by

$$\mathbf{r} = \mathbf{r}(\xi, \eta, \zeta, t) \,, \tag{6}$$

where $\mathbf{r} = (x, y, z)^T$ is the Cartesian coordinate system and t is the time. The computational domain (ξ, η, ζ) is divided into uniform primary cells with mesh size $\Delta\xi = \Delta\eta = \Delta\zeta = 1$, and the center of each primary cell is designated by the indices i, j, n. The area of the face l of a primary cell, see Fig. ??, is given by the vector quantity

$$\mathbf{S}^l = \frac{\partial \mathbf{r}}{\partial(l+1)} \times \frac{\partial \mathbf{r}}{\partial(l+2)} \,, \tag{7}$$

where the computational coordinates $l = \xi, \eta$ or ζ are in cyclic order and $\times$ is the cross product operator. The vector $\mathbf{S}^l$ has the magnitude of the face area and a direction normal to it. It is also the contravariant base vector ∇l scaled by the inverse of the Jacobian $1/J$, i.e., $\mathbf{S}^l = \frac{1}{J}\nabla l$, see[10].

Vinokur[10] has pointed out that an accurate discretisation should satisfy certain geometric identities. The condition that a cell is closed should be satisfied exactly in the discrete form

$$\sum_l \mathbf{S}^l = 0 \,, \tag{8}$$

where the summation (with proper signs) is over all the faces of the computational cell. Equation (8) can be satisfied if $\mathbf{S}^l$ is approximated from (7) by a proper approximation of $\frac{\partial \mathbf{r}}{\partial l}$ (see details in Ref. [8]). The volumes of all discrete computational cells will sum up to the total volume at a given time if the volume of each computational cell is computed by dividing the cell into three pyramids having in common the main diagonal and one vertex of the cell, resulting in the following

$$V = \frac{1}{3}\left(\mathbf{S}^{\xi}_{i-\frac{1}{2}} + \mathbf{S}^{\eta}_{j-\frac{1}{2}} + \mathbf{S}^{\zeta}_{n-\frac{1}{2}}\right) \cdot \left(\mathbf{r}_{i+\frac{1}{2},j+\frac{1}{2},n+\frac{1}{2}} - \mathbf{r}_{i-\frac{1}{2},j-\frac{1}{2},n-\frac{1}{2}}\right) \,. \tag{9}$$

In the present method, the volume conservation equation (4) is satisfied discretely by interpreting the term $d\mathbf{S} \cdot \mathbf{v}$ in equation (4) as the rate of the volume swept by the face $d\mathbf{S}$. For example the volume swept by the face $\mathbf{S}^{\xi}_{i+\frac{1}{2}}$ can be computed by a formula similar to (9)

$$(\delta V^{\xi}_{i-\frac{1}{2}})^{k+\frac{1}{2}} = \frac{1}{3}\left((\mathbf{S}^{\xi}_{i-\frac{1}{2}})^k + \delta\mathbf{S}^{\eta}_{j-\frac{1}{2}} + \delta\mathbf{S}^{\zeta}_{n-\frac{1}{2}}\right) \cdot \left(\mathbf{r}^{k+1}_{i-\frac{1}{2},j+\frac{1}{2},n+\frac{1}{2}} - \mathbf{r}^{k}_{i-\frac{1}{2},j-\frac{1}{2},n-\frac{1}{2}}\right) \tag{10}$$

where the time-level is given by k. The quantities $\delta S^{\eta}_{j-\frac{1}{2}}$ and $\delta S^{\zeta}_{n-\frac{1}{2}}$ are the areas swept by the motion of the face $S^{\xi}_{i-\frac{1}{2}}$ – see the shaded areas in Fig. ??. The area $\delta S^{\eta}_{j-\frac{1}{2}}$ is computed from

$$\delta S^{\eta}_{j-\frac{1}{2}} = \frac{1}{2}\left((\mathbf{r}^{k+1}_{n-\frac{1}{2}} - \mathbf{r}^{k}_{n+\frac{1}{2}}) \times (\mathbf{r}^{k+1}_{n+\frac{1}{2}} - \mathbf{r}^{k}_{n-\frac{1}{2}})\right)_{i-\frac{1}{2},j-\frac{1}{2}} \tag{11}$$

and $\delta S^{\zeta}_{n-\frac{1}{2}}$ can be computed in a similar way. The volume of the cell at the time level $k+1$ is computed from (4)

$$V^{k+1} = V^{k} + \sum_{l} (\delta V^{l})^{k+\frac{1}{2}} \quad , \tag{12}$$

where the summation (with the proper signs) is over all the faces of the computational cell. Note that $\delta V^{l}/\Delta t$ is the volume-flux due to the motion of the coordinate system and has a meaning similar to the volume-flux U^{l}. The computation of the volume of each cell at the time level $k+1$ as the sum of the volume at time level k and the contribution of the volumes δV^{l} swept out by the cell's faces is important for the accurate representation of the momentum equation.

In the present finite volume formulation, no coordinate derivatives appear directly in the discrete equations, as in the case of finite-difference formulas. Instead, quantities with clear geometric meaning such as the volume and faces area of the computational cells are used. Their discrete approximation is based on geometric interpretations which satisfy the geometric conservation laws. A principal difference between the finite volume and the finite difference approach to moving grids is in the interpretation of the quantity $\delta V^{l}/\Delta t$. In the finite-volume method it is treated as a geometric quantity which expresses the rate of displacement of a cell face, whereas in the finite-difference method, the grid velocity is combined with the fluid velocity to define a 'relative flow velocity' (see Ref. [10]).

3.2 Mass Conservation Equation

The mass conservation equation (5) has the same form as for fixed grids. Second-order spatial discretisation over the faces of the primary computational cells yields

$$\begin{aligned}(\mathbf{S}^{\xi}\cdot\mathbf{u})_{i+\frac{1}{2}} - (\mathbf{S}^{\xi}\cdot\mathbf{u})_{i-\frac{1}{2}} + (\mathbf{S}^{\eta}\cdot\mathbf{u})_{j+\frac{1}{2}} - (\mathbf{S}^{\eta}\cdot\mathbf{u})_{j-\frac{1}{2}} \\ + (\mathbf{S}^{\zeta}\cdot\mathbf{u})_{n+\frac{1}{2}} - (\mathbf{S}^{\zeta}\cdot\mathbf{u})_{n-\frac{1}{2}} = 0 \end{aligned} \tag{13}$$

Note that throughout the present paper the default indices (i,j,n) and the default time-level $(k+1)$ are usually omitted for simplicity. Each term on the left hand side of (13) approximates the volume-flux over a face of the primary cell. A simple discretised mass conservation equation can be obtained by using the following variables

$$\begin{aligned} U^{\xi} &= \mathbf{S}^{\xi}\cdot\mathbf{u}\,, \\ U^{\eta} &= \mathbf{S}^{\eta}\cdot\mathbf{u}\,, \\ U^{\zeta} &= \mathbf{S}^{\zeta}\cdot\mathbf{u}\,, \end{aligned} \tag{14}$$

as the unknowns instead of the Cartesian velocity components. The quantities U^{ξ}, U^{η} and U^{ζ} are the volume-fluxes over the ξ, η and ζ faces of a primary cell, respectively. In tensor algebra nomenclature, these are the contravariant components of the velocity vector (in a staggered grid) scaled by the inverse of the Jacobian $(1/J)$. With this choice of the dependent variables, the continuity equation takes a form identical to the Cartesian case

$$U^{\xi}_{i+\frac{1}{2}} - U^{\xi}_{i-\frac{1}{2}} + U^{\eta}_{j+\frac{1}{2}} - U^{\eta}_{j-\frac{1}{2}} + U^{\zeta}_{n+\frac{1}{2}} - U^{\zeta}_{n-\frac{1}{2}} = 0\,. \tag{15}$$

Accumulated experience with fractional step solution methods shows that the exact satisfaction of the discrete mass conservation equation is crucial for obtaining accurate solutions and for the convergence of the Poisson equation, see for example Ref. [11]. Therefore, the simple form of (15), which can be satisfied to round-off errors in any coordinate system, suggests that the volume-fluxes are the 'natural' dependent variables for fractional step methods. This choice complicates the discretisation of the momentum equations, but is important for obtaining a divergence-free velocity field in generalised coordinate systems.

3.3 Momentum conservation equation

Spatial discretisation of the momentum conservation law (2) for a computational cell with volume V yields

$$\frac{\partial}{\partial t}(V\,\mathbf{u}) = \sum_{l} \mathbf{S}^{l}\cdot\bar{T} = \mathbf{F}\,. \tag{16}$$

Following the development of the scheme given by Rosenfeld *et al.*[8], a general two-step temporal discretisation of (16) for a constant time-step Δt is

$$\begin{aligned}(1+\epsilon)(V\mathbf{u})^{k+1} - (1+2\epsilon)(V\mathbf{u})^{k} + \epsilon(V\mathbf{u})^{k-1} \\ = \Delta t(\theta\mathbf{F}^{k+1} + (1-\theta)\mathbf{F}^{k} + \phi(\mathbf{F}^{k} - \mathbf{F}^{k-1}))\,, \end{aligned} \tag{17}$$

where k is the time level and ϵ, θ and ϕ are arbitrary parameters. A truncation error analysis shows that second-order accuracy in time is obtained only if

$$\frac{1}{2} + \epsilon = \theta + \phi\quad . \tag{18}$$

In order to replace $\mathbf{u}$ by the new dependent variables U^{l}, the corresponding area vectors are dotted with the momentum equations. The integral momentum equation is applied on different computational cells for each unknown U^{l}. Each cell has the dimensions $\Delta\xi \times \Delta\eta \times \Delta\zeta$, but the centers are located at $(i+\frac{1}{2}, j, n)$, $(i, j+\frac{1}{2}, n)$ and $(i, j, n+\frac{1}{2})$ for the U^{ξ}, U^{η}, and U^{ζ} momentum equations, respectively. The derivation of the ξ-momentum equation

will be described in this section. The other two momentum equations can be obtained by cyclic permutation.

The dependent variables are the pressure and the volume-fluxes (see 3.2). In order to replace the unknown $\vec{u}$ by U^l, eq. (17) is dotted by S^ξ and using the identity

$$u = S_\xi U^\xi + S_\eta U^\eta + S_\zeta U^\zeta = S_m U^m \qquad (19)$$

results in

$$(1+\epsilon)(V\,U^\xi)^{k+1} - (1+2\epsilon)(V\,U^l)^k(S^\xi \cdot S_l^k) + \epsilon(V\,U^l)^{k-1}(S^\xi \cdot S_l^{k-1}) \qquad (20)$$
$$= \Delta t(\theta S^\xi \cdot F^{k+1} + (1-\theta)S^\xi \cdot F^k + \phi S^\xi \cdot (F^k - F^{k-1}))$$

where S_m is the inverse base of S^l. Note that the $k+1$ is the default time-level and therefore S^ξ is computed at $k+1$. In order to save computations, only the term $L = S^\xi \cdot F$ at the time-levels $k-1, k$, and $k+1$ should appear in (20). Therefore, the right hand side of (20) is modified to

$$\frac{RHS(20)}{\Delta t} = \theta(S^\xi \cdot F)^{k+1} + (1-\theta)(S^\xi \cdot F)^k + \phi(S^\xi \cdot F)^k - (S^\xi \cdot F)^{k-1}) \qquad (21)$$
$$= \theta L^{k+1} + (1-\theta)L^k + \phi(L^k - L^{k-1}) \ .$$

This approximation is first-order in time. The temporal truncation errors can be minimised by choosing $\epsilon = \frac{1}{2}$ and $\phi = 1-\theta$. The resulting scheme is

$$3(V\,U^\xi)^{k+1} - 4(V\,U^l)^k(S^\xi \cdot S_l^k) + (V\,U^l)^{k-1}(S^\xi \cdot S_l^{k-1})$$
$$= 2\Delta t(\theta L^{k+1} + (1-\theta)(2L^k - L^{k-1})) \ . \qquad (22)$$

For stability reasons, usually $\theta = 1$ is chosen.

The computation of the operator L is similar to the fixed grid case and details can be found in[8,9]. The only difference is in the computation of the convection terms which should include the motion of the grid. For example, the convection flux of the ξ-momentum equation on the ξ-face center (i,j,n) is given by

$$\left(-(U^\xi - \frac{\delta\mathcal{V}^\xi}{\Delta t})U^l S_l\right)_{i,j,n} \ .$$

The difference equations could have been second-order accurate in time if $\delta\mathcal{V}^\xi$ would not lag in time by $\frac{\Delta t}{2}$ over the volume-flux terms U^l (see eq. (10)).

The resulting discrete equations are conservative in any moving coordinate system and are spatially second-order accurate. For high Reynolds number flows, fourth-order dissipation is added to annihilate high frequency components of the solution. The dissipation terms are interpreted in terms of fluxes and therefore the conservation properties of the equations are maintained.

4 Solution Method

The dependent variables are the pressure, defined at the center of the primary cells, and the volume-fluxes defined on the faces of the primary cells. This selection is equivalent to a finite-difference formulation over a staggered grid with the choice of scaled contravariant velocity components as the unknowns. The mass and momentum conservation equations (5) and (22) are solved by a fractional step method. First the momentum equations are solved for an approximate U^l by an approximate factorisation method. In the second stage, the pressure and the volume-fluxes U^l are corrected to satisfy the mass conservation equation by solving a Poisson equation. It should be noted that the exact satisfaction of the discrete mass conservation equation ensures the convergence of the Poisson equation with good convergence properties. More details on the solution method can be found in Refs. [8,9].

The original solution method used an explicit approximation of the convection terms. In the present implementation, the most important convection terms may be approximated also implicitly and therefore the scheme has no severe restrictions on the allowable CFL-number. Explicit or implicit fourth-order dissipation can be used for high Reynolds number flows.

5 Results

Several test cases have been solved so far. The solution procedure and the computer-code are capable of solving three-dimensional flowfields, but at this stage of the study only two-dimensional cases have been considered.

5.1 Flow over a Circular Cylinder

The flowfield over a circular cylinder at $Re = 40$ was solved as the first test case. This example is a common test case for fixed grid solutions since the resulting flowfield is quite complicated and numerous other numerical and experimental results are available for comparison. In the present solution, the grid is expanding radially due to a moving circular outer boundary

$$R_{max}(t) = 7 + \frac{4}{3}t - \frac{t^2}{24} \ , \qquad (23)$$

where R_{max} is the distance of the outer boundary from the cylinder center (normalised with the cylinder's diameter). In the present case the dependence of the grid on time is pre-determined. However, the same procedure may be used to solve a time-dependent problem by an adaptive-grid method, if a suitable adaptation criterion would have been defined.

A cylindrical coordinate system is used with mesh points clustered near the cylinder and in the wake region.

Figure ?? gives the grid and the instantaneous streamlines for $t = 1$ and $t = 8$. Between the times shown, the radial mesh size is almost doubled in size. Nevertheless, the time-evolution of the separation bubble, which is a critical test parameter, agrees well with previous numerical and experimental results, see Fig. ??. The full line in Fig. ?? describes the solution obtained in the this study while the dashed line gives the solution obtained by the fixed-grid version of the present method. The triangular symbols and the dotted line give the experimental results of Coutanceau and Bouard[12] and the numerical solution of Collins and Dennis,[13] respectively. All the results practically coincide, except the numerical results of[13] for $t > 7$. As was explained by Rosenfeld *et al.*,[8] this deviation results mainly from the "wall effect." Note especially the good agreement with the experimental results which have been obtained for an equivalent outer boundary of about 14 diameters. This is about the same as the outer boundary distance in the present computations at $t \approx 8$.

5.2 Channel Flow with an Asymmetric Oscillating Indentation

This test case considers the flowfield in a two-dimensional channel with an oscillating constriction. This geometry is a model for the large amplitude self-excited oscillations that arise when fluid flows through a collapsible tube such as a vein. In a series of flow visualisations, Stephanoff *et al.*[14] and Pedley and Stephanoff[15] have found in the core of the flow a train of waves, downstream of the oscillating indentation, and a double row of eddies along the walls of the channel.

In the experimental apparatus the walls of the channel were rigid except for an indentation of length 10 (the distance between the fixed parts of the walls is the reference unit length). The indentation is made of a thick rubber membrane and is driven by a piston with a sinusoidal motion with time. At the begining of each cycle, the indentation is flushed with the channel's wall. The channel starts at a distance of 120 units upstream of the oscillating constriction and is 250 units long. The flowfield upstream of the indentation is fully developed and the flow is essentially laminar.

In the present work a simplified model of the test apparatus is employed. The upstream boundary is at a distance of 5 units from the oscillating constriction and the downstream boundary is at a distance of 30 units from the upstream boundary. An algebraic grid is generated at each time step with $31 \times 251 \times 3$ points along the heigth, length and width of the channel, respectively. Points are clustered near the two walls and a non-uniform distribution of points is used in the axial direction with clustering in the region downstream of the indentation where the flow structure was found experimentally to be most interesting. The mesh points are fixed in time except at the indentation region where mesh points stretch linearly with the the distance between the moving indentation and the opposite fixed wall. The maximum indentation is 0.38 units. The grid for this position is shown in Fig. ??, where only every other point is plotted in the normal and axial directions and the vertical scale is twice as large as the axial scale. The shape of the indentation is approximated by a hyperbolic tangent, as has been suggested by Pedley and Stephanoff[15] and Ralph and Pedley.[7] The apparent asymmetry of the indentation is a result of the non-uniform grid used in the present case. It was found in Ref. [7], as well as in the computations performed in this study, that the flowfield downstream of the indentation is not sensitive to the upstream conditions.

Fully developed flow is given as the initial condition and as the upstream boundary condition. The downstream condition imposes parallel flow and a uniform pressure gradient which is computed from the integral mass conservation law. At the upper and lower walls, the velocity of the wall is specified (zero everywhere, except at the moving parts of the boundary).

Figure ?? shows a comparison of the instantaneous streamlines with a flow visualisation of Stephanoff *et al.*[14] at the non-dimensional time of $t = 0.55$ (based on the period) and for a case with a Strouhal number of $St = 0.038$ and a Reynolds number of $Re = 610$. The flow visualisation shows quite a complicated flowfield although the resolution is not good enough for revealing the fine details, especially in the regions of eddy motion. The first separation of the flow occurs downstream of the sloping wall. A second large eddy is formed on the opposite wall with a secondary separation bubble buried inside it. Still further downstream, an additional pair of weaker vortices appear, one on each wall. The core of the flow prescribes a wave motion which can be observed easily both in the experimental and the numerical results.

Favorable agreement can be obtained if the plot of the numerical result is moved about 0.4 units in the downstream direction relative to the experimental results. In other words, the separation length of the first eddy at the upper-wall is under-predicted in the present computations. Nevertheless, the distances between the vortices, which are related to the wavelength of the core-flow, compare favorably. The reason for this discrepancy is not clear and requires additional study. The differences do not seem to be related to the resolution since grid refining does not affect the separation length significantly. Kiris and Rogers[6] has solved the same case with a high-order upwind scheme and found similar results. The fact that two solution procedures, which differ in numerous aspects, result in similar solutions can indicate that the differences may be related to the non-exact reproduction of the experimental set-up and conditions.

One very likely reason for the discrepancy may be at-

tributed to three-dimensional effects. In the present computations a two-dimensional flow is assumed. In the experiments conducted by Stephanoff *et al.*[14] the width of the channel was 10 times larger than its height. The three-dimensional affects of the sidewalls on the centerplane, where the visualisations were taken, could not be assessed. Armaly *et al.*[16] have investigated experimentally the steady flow past a backward-facing step and found three-dimensional effects for $Re > 400$. The most sensitive quantity was the length of the separated eddies. In unsteady flows, the three-dimensional effects are even more pronounced, see for example Ref. [17]. Another reason for the disagreement could be the inaccurate description of the wall shape in the numerical computations. Obviously, any difference in the shape may affect the length of the separation from the indentation.

The flow evolution for $Re = 600$ and a higher Strouhal number, $St = 0.057$, is given in Fig. ??. Here the instantaneous streamlines are plotted for several non-dimensional times at the first cycle of the indentation's motion. The flow development is essentially the same as that found experimentally by Pedley and Stephanoff[15] and is summarised only briefly here.

Near the beginning of the cycle, a single separation bubble forms on the sloping wall of the indentation (Fig. ??a) and the core-flow remains parallel to the walls. As time increases, the separation length increases and a second counter-rotating eddy appears on the opposite wall, downstream of the first eddy – see Fig. ??b. Still later, a third eddy is formed at the upper wall further downstream (Fig. ??c). As time proceeds, the core-flow becomes wavy and a sequence of eddies with alternating signs appear on the walls. The amplitude of the core-flow increases with time until $t = 0.75$ (Fig. ??g). In the last quarter of the period, the eddies shrink in size and strength and are washed downstream. At the end of the cycle the residual eddies are quite small and do not affect the next cycle. We shall adopt the convention of Ref. [15] in labeling the eddies alphabetically, as shown in Fig. ??d.

Of particular interest is the phenomenon of eddy-doubling which was found experimentally (Ref. [15]) as well as computationally (Ref. [7]). In this phenomenon, a single eddy splits into two *co-rotating* eddies. The present calculations show that eddy-doubling occurs for eddies A, B and C for $t > 0.55$.

The genesis of the wavy flow as well as the mechanism of the eddy-doubling is still not fully understood. Most previous studies agree that the wavy core-flow is determined primarily by inviscid vorticity dynamics and is a result of the non-zero vorticity gradient, see Refs. [7,15,17]. It is also clear that the eddy-doubling is essentially a viscous bifurcation, Refs.[7,15]. The motivation of the present paper is to describe the numerical solution procedure, therefore no further attempt will be made to analyse this flowfield.

Figure ?? plots the center of the vortices A, B, C and D (which approximately coincides with the crests and troughs of the core flow streamlines) as a function of time for four different results. The experimental results are given by square symbols while the various numerical computations are represented by lines. The numerical results include the present study (full lines)as well as the computations of Kiris and Rogers[6] (dash lines) and Ralph and Pedley[7] (dotted lines). The agreement between the present results and the results obtained by Kiris and Rogers is good, except perhaps for the first separated eddy (A). The numerical results of Ralph and Pedley,[7] who used a stream-function-vorticity formulation and a mesh with about 3.5 times more points in the axial direction, show better agreement with the experimental results, obviously due to the better prediction of the first separation length. However, the *distances* between the vortices (or the wavelength) compare favorably between all these results.

5.3 Internal Flow Driven by a Piston

The last case demonstrates the capabilities of the present numerical procedure. In this case, a two-dimensional internal flow in a rectangular cavity driven by a vertically pulsating piston is solved for a Reynolds number Re=100, see geometry in Fig. ??. During the downward stroke of the piston, the fluid leaves through an exit at the left vertical wall, and during the upward motion the entrance at the right vertical wall opens and the exit is closed. This flowfield is an idealisation of a reciprocal engine or an artificial heart. The piston has a sinusoidal motion between $y = 0.6$ and $y = 0.3$ with a period of 1.2 non-dimensional seconds.

An algebraic grid of $49 \times 45 \times 3$ points in the x, y and z directions, respectively has been employed. Mesh points are clustered near the two side walls and near the lower wall. Along the y-direction, the mesh points are stretched linearly with the motion of the piston. The x-direction distribution remains fixed. Figure ?? shows the time evolution of the force-coefficients in the y and x directions on the lower stationary horisontal wall (opposing the piston). A fully developed periodic flow is seen to persist from the second cycle of the piston. The abrupt closing of the exit (at $t = 0.6, 1.8, 3.$, etc.) and the abrupt closing of the entrance (at $t = 1.2, 2.4, 3.6$, etc.) can be clearly observed as a sharp change in the x-component of the force-coefficient.

Figure ?? gives the velocity vector and the pressure contours for the fifth cycle. The velocity vector is plotted for every other mesh point in both x and y directions. At the beginning of the cycle a strong vortex, which was created in the previous cycle near the entrance, is found along with a contra-rotating weaker vortex. At half stroke

downward, no vortices exist (except very weak vortices near the two lower corners). A very strong pressure gradient builds up at the exit. As the entrance opens, Fig. ??c, two main vortices are found in the core region, but they are weaker than at the beginning of the cycle. During the upward motion of the piston, a strong vortex is generated at the entrance, Fig. ??d. A favorable agreement has been found with Kiris and Rogers,[6] who has solved the same case by a time-accurate artificial compressibility method with high-order upwinding.

6 Concluding Remarks

A general solution method of the time-accurate incompressible Navier-Stokes equations in a generalised curvilinear moving coordinate system is presented. Accuracy is achieved by employing conservative finite-volume discretisation with special attention to the satisfaction of geometric conservation laws in generalised moving coordinate systems. A fractional step solution method is used to efficiently solve the discrete equations. The pressure and the *volume-fluxes* are chosen to be the independent variables. This choice simplifies the construction of a robust Poisson solver. The present method is an alternative to other finite difference methods.

Several test solutions show promising results. It is especially encouraging to obtain smooth solutions near inflow and outflow boundaries which are time dependent. Future work will include the solution of more realistic three-dimensional cases with moving boundaries as well as time-dependent problems with self-adaptive grids.

References

[1] Kwak, D., Chang, J. L. C. , Rogers, S. E. and Rosenfeld, M., "Three-Dimensional Incompressible Navier-Stokes Computations of Internal Flows", Proc. of the 12th IMACS World Congress on Scientific Computation, Paris, France, July 18-22, 1988, (also NASA TM 100076, March 1988).

[2] Ogawa, S. and Ishiguro, T., "A method for Computing Flow Fields around Moving Bodies", *J. Comp. Phys.*, 69, 1987, pp. 49–68.

[3] Tamura, T., Tsuboi, K. and Kuwahara, K., "Numerical Simulation of Unsteady Flow Patterns around a Vibrating Cylinder","AIAA-88-0128.

[4] Rogers, S. E. and Kwak, D., "Numerical Solution of the Incompressible Navier-Stokes Equations for Steady-State and Time-Dependent Problems," AIAA-89-0463, 1989.

[5] Rogers, S. E. and Kwak, D., "An Upwind Differencing Scheme for the Time-Accurate Incompressible Navier-Stokes Equations", AIAA-88-2583.

[6] Kiris, C., and Rogers, S. E., Private Communication, September 1988.

[7] Ralph, M. E. and Pedley, T. J., "Flow in a Channel with a Moving Indentation", *J. Fluid Mechanics*, 190, 1988, pp. 87–112.

[8] Rosenfeld, M., Kwak, D. and Vinokur, M., "A Solution Method for the Unsteady and Incompressible Navier-Stokes Equations in Generalised Coordinate Systems", AIAA-88-0718.

[9] Rosenfeld, M., Kwak, D. and Vinokur, M., "Development of an Accurate Solution Method for the Unsteady Incompressible Navier-Stokes Equations in Generalised Coordinate Systems", NASA TM, to appear, 1989.

[10] Vinokur, M., "An Analysis of Finite-Difference and Finite-Volume Formulations of Conservation Laws", NASA CR-177416, June 1986.

[11] Gresho, M. P. and Sani, R. L., "On Pressure Boundary Conditions for Incompressible Navier-Stokes Equations", *Int. J. Numerical Methods in Fluids*, 7, 1987, pp. 1111–1145.

[12] Bouard, R. and Coutanceau, M., "The Early Stage of Development of the Wake Behind an Impulsively Started Cylinder for $40 < Re < 10^4$", *J. Fluid Mechanics*, 101, 1980, pp. 583–607.

[13] Collins, W. M. and Dennis, S. C. R., "Flow Past an Impulsively Started Circular Cylinder", *J. Fluid Mech.*, 60, 1973, pp. 105-127.

[14] Stephanoff, K. D., Pedley, T. J., Lawrence, C. J. and Secomb, T. W., "Fluid Flow along a Channel with an Asymmetric Oscillating Constriction", *Nature*, 305, 1983, pp. 692–695.

[15] Pedley, T. J. and Stephanoff, K. D., "Flow along a Channel with a Time-dependent Indentation in One Wall: the Generation of Vorticity Waves", *J. Fluid Mechanics*, 160, 1985, pp. 337–367.

[16] Armaly, B. F., Durst, F., Pereira, J. C. T. and Schonung, B., "Experimental and Theoretical Investigation of Backward-Facing Step Flow", *J. Fluid Mech.*, 127, 1983, pp. 473-496.

[17] Sobey, I. J., "Observation of Waves During Oscillatory Channel Flow", *J. Fluid Mech.*, 151, 1985, pp. 395-426.

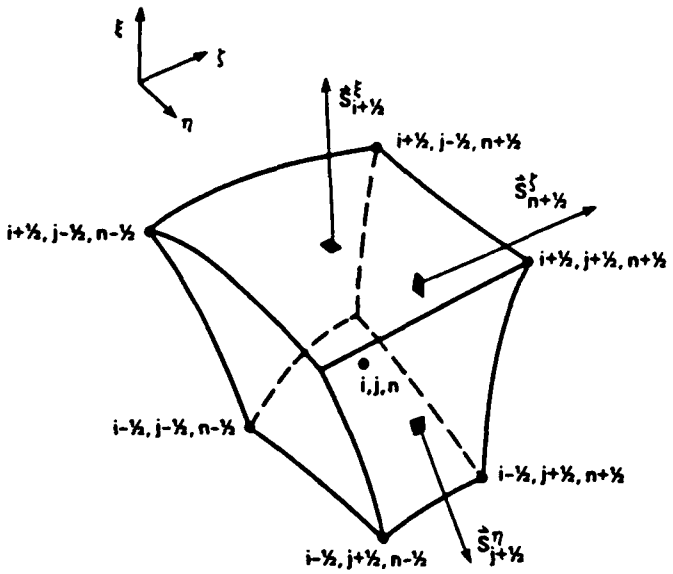

Figure 1: The definition of the primary cell

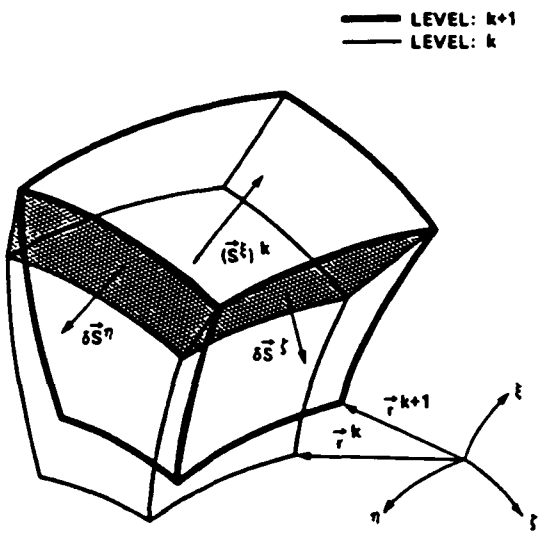

Figure 2: Definitions related to moving grids

$$T = 1 \quad , \quad R_{max} = 8.29$$

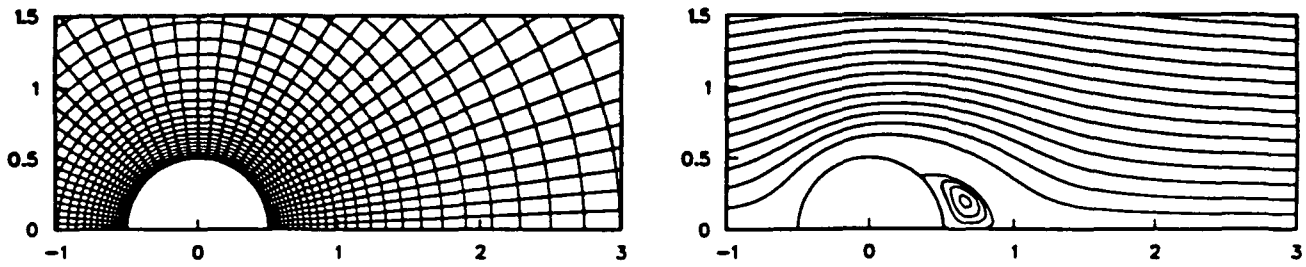

$$T = 8 \quad , \quad R_{max} = 15.00$$

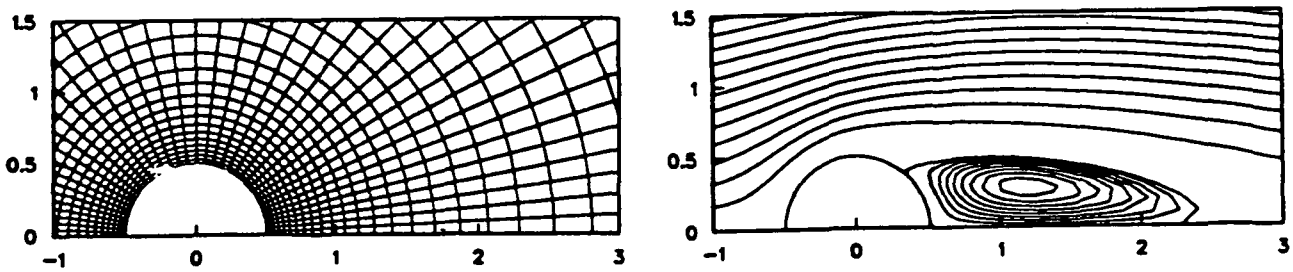

Figure 3: The grid and the instantaneous streamline contours for $t = 1$ and $t = 8$

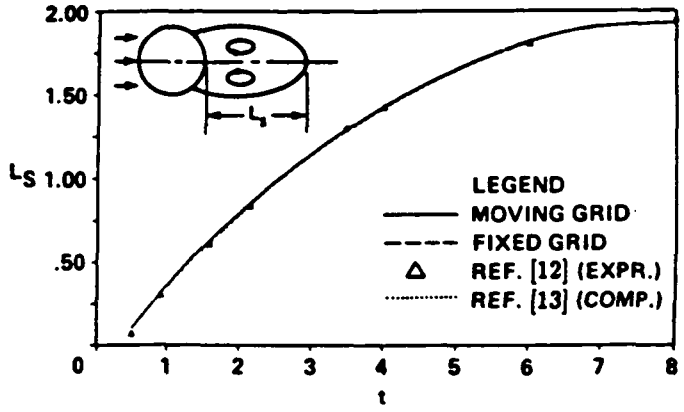

Figure 4: Time-evolution of the separation length over a circular cylinder at $Re = 40$

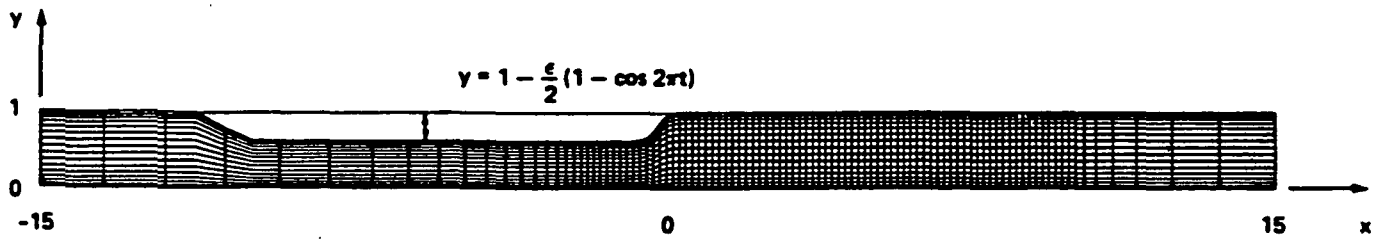

Figure 5: The grid for the channel flow with oscillating indentation

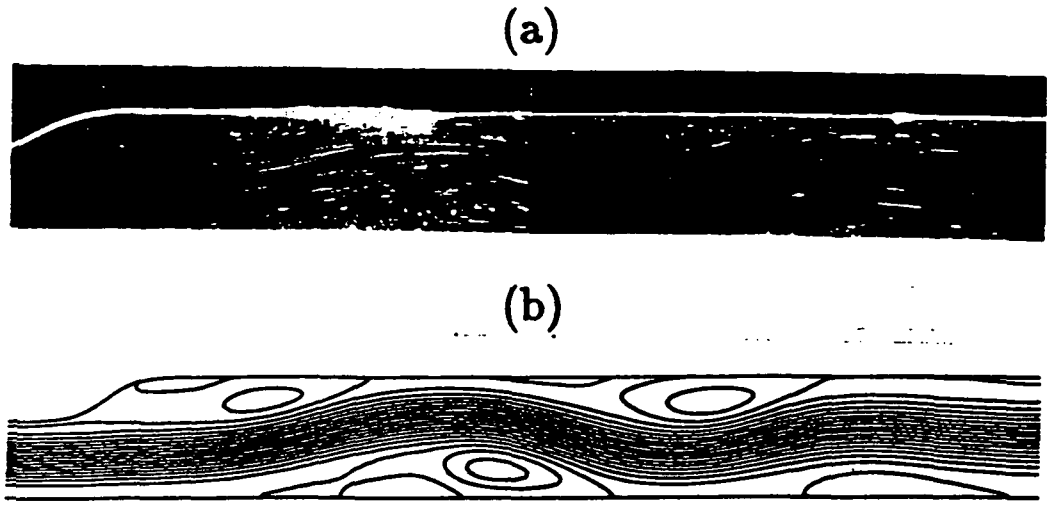

Figure 6: Comparison of the instantaneous streamlines at $t = 0.55$ and $St = 0.038$, $Re = 610$. (a) experimental results (b) present results

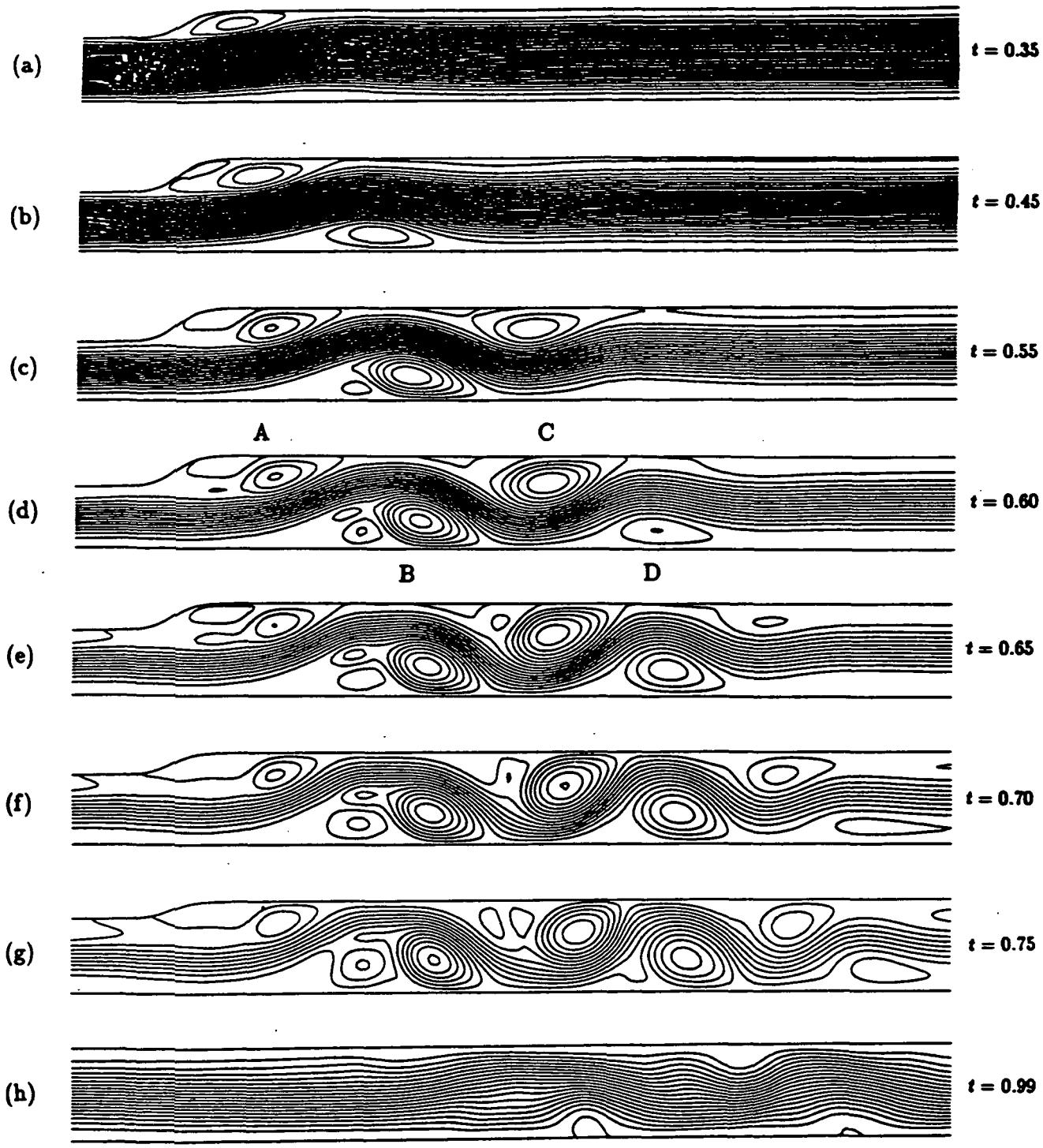

Figure 7: Instantaneous streamlines, $St = 0.057$, $Re = 600$

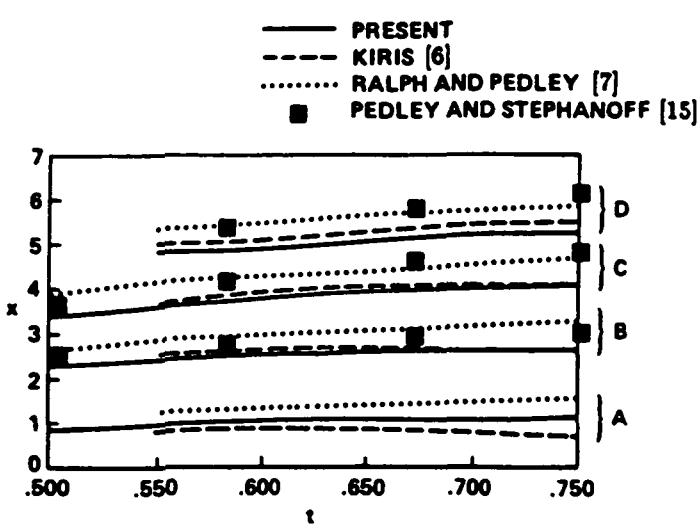

Figure 8: Time evolution of the vortices center

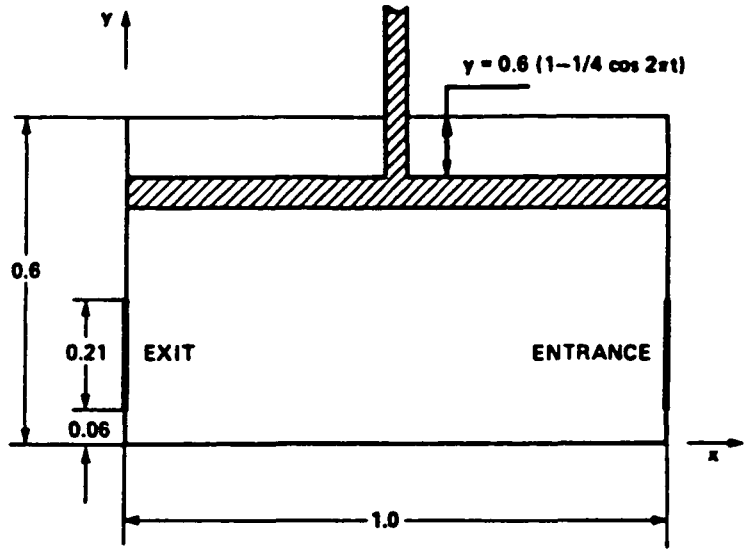

Figure 9: The geometry of the piston flow case

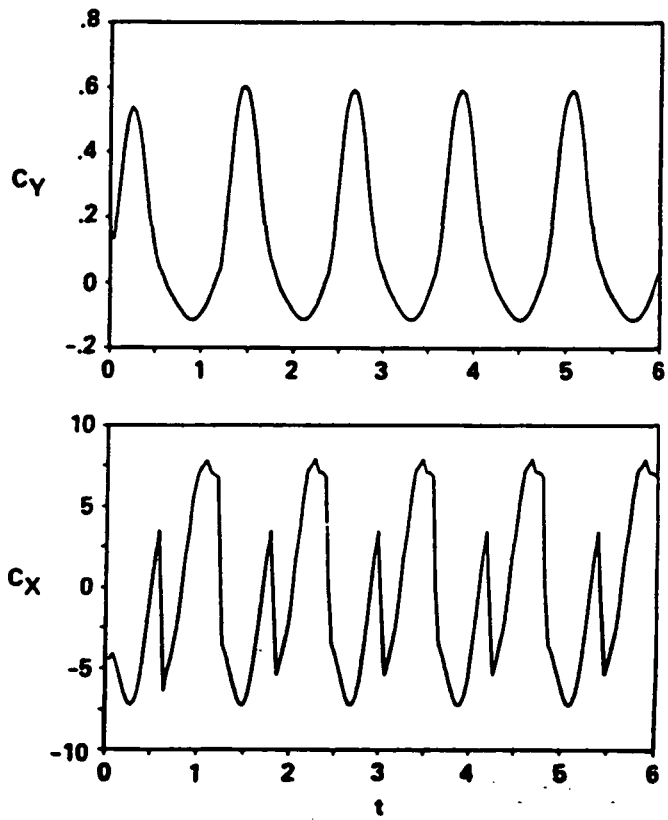

Figure 10: Time-evolution of the force-coefficients on the lower wall

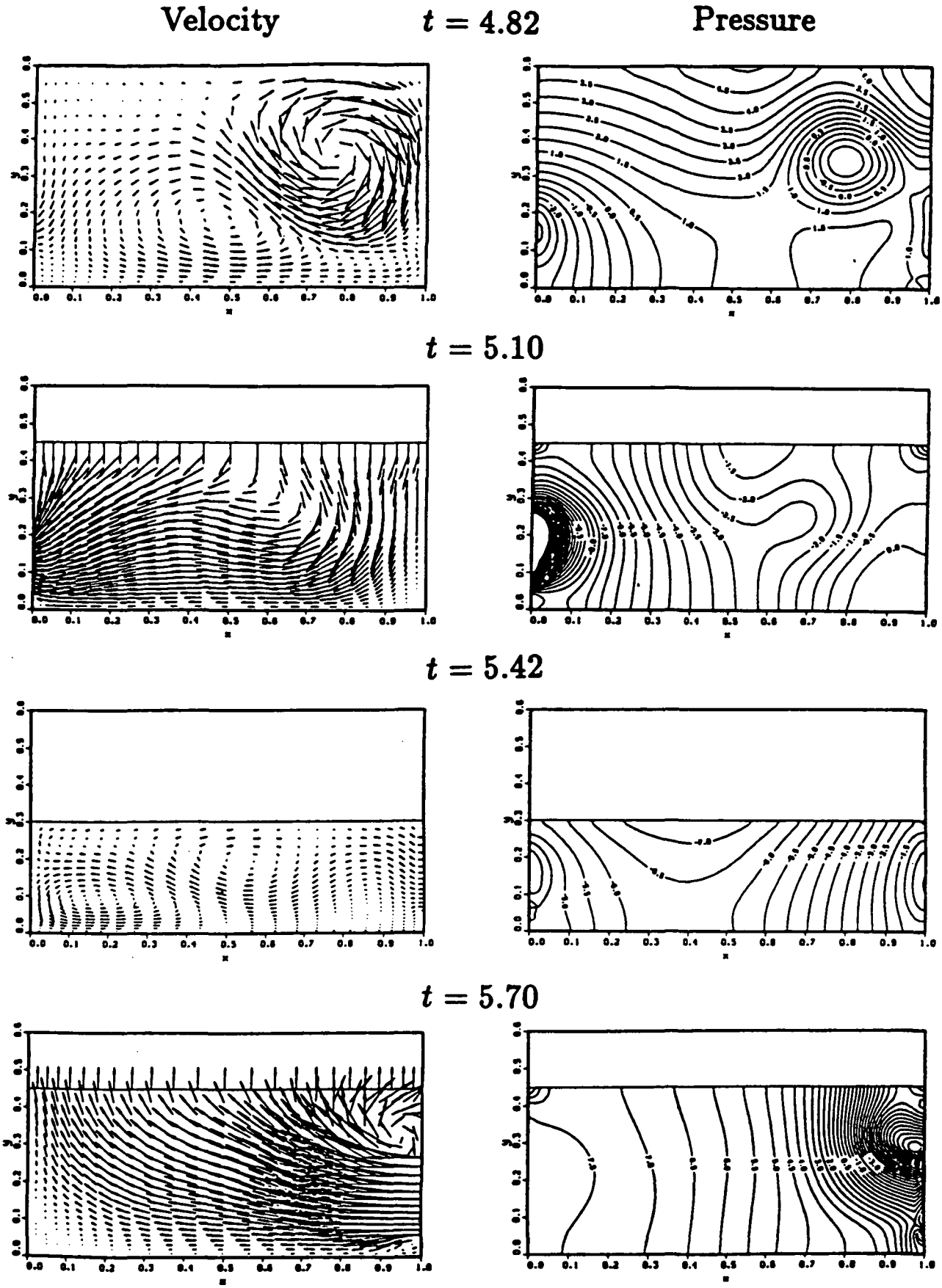

Figure 11: Velocity vector and pressure contours